OPTICA

Inverse design of spontaneous parametric downconversion for generation of high-dimensional qudits

Eyal Rozenberg,[1,*] **Aviv Karnieli,**[2] **Ofir Yesharim,**[3] **Joshua Foley-Comer,**[3] **Sivan Trajtenberg-Mills,**[2,4] **Daniel Freedman,**[5] **Alex M. Bronstein,**[1] **and Ady Arie**[3]

[1] *Department of Computer Science, Technion, Haifa, Israel*
[2] *Raymond and Beverly Sackler School of Physics and Astronomy, Tel Aviv University, Israel*
[3] *School of Electrical Engineering, Fleischman Faculty of Engineering, Tel Aviv University, Israel*
[4] *Massachusetts Institute of Technology, Cambridge, Massachusetts 02139, USA*
[5] *Google Research, Haifa, Israel*
**Corresponding author: eyal.rozenberg1@gmail.com*

Received 10 December 2021; revised 25 April 2022; accepted 27 April 2022; published 6 June 2022

Spontaneous parametric downconversion (SPDC) in quantum optics is an invaluable resource for the realization of high-dimensional qudits with spatial modes of light. One of the main open challenges is how to directly generate a desirable qudit state in the SPDC process. This problem can be addressed through advanced computational learning methods; however, due to difficulties in modeling the SPDC process by a fully differentiable algorithm, progress has been limited. Here, we overcome these limitations and introduce a physically constrained and differentiable model, validated against experimental results for shaped pump beams and structured crystals, capable of learning the relevant interaction parameters in the process. We avoid any restrictions induced by the stochastic nature of our physical model and integrate the dynamic equations governing the evolution under the SPDC Hamiltonian. We solve the inverse problem of designing a nonlinear quantum optical system that achieves the desired quantum state of downconverted photon pairs. The desired states are defined using either the second-order correlations between different spatial modes or by specifying the required density matrix. By learning nonlinear photonic crystal structures as well as different pump shapes, we successfully show how to generate maximally entangled states. Furthermore, we simulate all-optical coherent control over the generated quantum state by actively changing the profile of the pump beam. Our work can be useful for applications such as novel designs of high-dimensional quantum key distribution and quantum information processing protocols. In addition, our method can be readily applied for controlling other degrees of freedom of light in the SPDC process, such as spectral and temporal properties, and may even be used in condensed-matter systems having a similar interaction Hamiltonian.

https://doi.org/10.1364/OPTICA.451115

1. INTRODUCTION

The penetration of advanced machine learning (ML) methods into physics has led to far-reaching advances in both theoretical predictions and experiments, yielding exciting and interesting new results [1–6]. Some of the most interesting progress has come from the solution of inverse problems [7] aimed at finding novel experimental setups that produce a desired physical observable [8–18]. Nevertheless, there are still physical phenomena, particularly in quantum physics, that have not yet benefited from this progress. This may be attributed at least partially to the lack of appropriate computational tools for modeling complex quantum systems, and in some cases to the stochastic dynamics involved in modeling quantum phenomena such as spontaneous processes and fluctuations of quantum fields [19–25].

One important branch of quantum physics that might benefit significantly from the adoption of inverse design algorithms is quantum optics [26,27]. Quantum optics has proven to be an invaluable resource for the realization of many quantum technologies, such as quantum communication [28–31], quantum computing [32–35], and cryptography [36–40]. A prominent reason for this is the availability of sources for generating nonclassical light [27], which are mainly based on nonlinear interactions [41]. The most prevalent of these processes is spontaneous parametric downconversion (SPDC) in second-order nonlinear $\chi^{(2)}$ materials [42]. The nonlinear coefficient of ferroelectric materials can be modulated by electric field poling in two out of the three crystal axes [43,44]. Recently, this capability was extended to enable modulation in all three axes using focused laser beams [45–53]. 3D nonlinear photonic crystals (NLPCs) offer a promising new avenue for shaping and controlling arbitrary quantum correlations between photons. This new technology introduces additional degrees of freedom for tailoring the quantum state of structured

2334-2536/22/060602-14 Journal © 2022 Optica Publishing Group

photon pairs [54–62]. Solving the inverse quantum optical design would make it possible to find the optimal physical parameters of the system, such as the pump beam profile and the 2D or 3D NLPC structures that yield the desired quantum state. These capabilities can be used for the generation of maximally entangled photonic states of arbitrary dimensionality that allow stronger violation of generalized Bell's inequalities, the encoding of larger capacities of quantum information on light [63], and improved security in quantum key distribution [38,64,65].

If we wish to employ learning-style optimization methods for problems in quantum optics, it is crucial to have a good physical model of the quantum optical process in question and integrate it into the algorithm itself [2,3,6,15,66–69]. The model should ideally encompass the relevant conservation laws, physical principles, and phenomenological behaviors. Such physically constrained models will ensure convergence to physically realizable solutions, reduce the parameter search, improve the predictive accuracy and statistical efficiency of the model, and allow for faster training with improved generalization. However, there are obstacles to incorporating learning-style optimization methods into quantum optics while still properly capturing the physics. To account for general optical medium geometry, diffraction, dispersion, and non-perturbative effects in non-classical light generation (such as SPDC), accurate simulation schemes must be employed that go beyond the scope of the more frequently used analytic calculations [42,54,7071,]. However, such models—which are more appealing for the inverse design of complex optical media—are often stochastic [20,25,71,]. The stochastic nature of the problem, also prominent in other physical fields such as those that employ Monte Carlo simulations [72], makes modern descent-based algorithms difficult to employ.

In this paper, we provide an algorithm that yields promising results in the inverse design problem of generating structured and entangled photon pairs in quantum optics using tailored nonlinear interactions in the SPDC process. The learned interaction parameters can then be used to predict the generation of the desired quantum state or correlations between structured photon pairs in future experiments, as illustrated in Fig. 1. Our SPDCinv model is derived from Heisenberg's equations of motion for quantum fields, is non-perturbative (can be used to simulate high-gain effects), and can learn many important parameters of the quantum optical process necessary for generating arbitrarily shaped correlated photon pairs. We show how to make an inherent stochastic description of SPDC fully differentiable, making it amenable to descent-based methods of optimization. Furthermore, we use a split-step Fourier (SSF) method [73] to solve our forward model. To the best of our knowledge, this is the first time that a differentiable model has been integrated with SSF—a feature also relevant for many other inverse problems in optics and quantum mechanics (it combines diffraction, or more generally, propagation, in space, to solve nonlinear partial differential equations, such as the nonlinear Schrödinger equation). Our forward model has already been validated against a number of published experimental results, detailed in [25,74,75], for the cases of structured pump beams [57,59,76] and structured crystals [25,74,75]. In this paper, we further validate it against other experiments [57,20], obtaining very good agreement for both on-axis spatial mode correlations, as well as to the quantum state tomography (QST) of the generated state. Moreover, we demonstrate the full process of inverse design to obtain the correct relations between crystal length and pump waist, as achieved in the experiments [57].

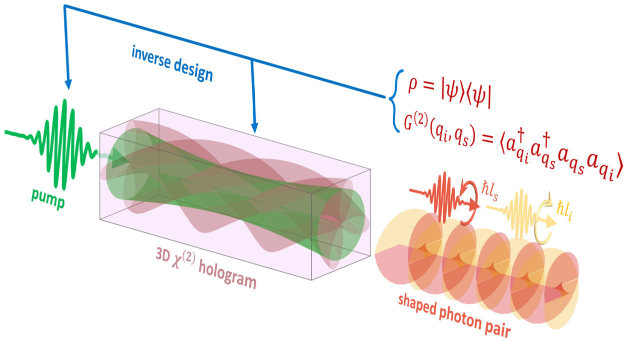

Fig. 1. Illustration of the inverse design problem. Given the desired coincidence rate counts, $G^{(2)}$, and density matrix, ρ, the SPDCinv algorithm solves the inverse design problem and extracts the optimal 3D NLPC structure and the complex pump beam structure, for generating the desired quantum state of the spontaneously emitted structured photon pairs.

We use our model to discover the optimal NLPC structures (2D NLPCs [43,44,77–82] or 3D NLPCs [45–53]) and the pump structures that generate desired nontrivial quantum correlations (coincidence rate counts) and quantum states (bi-photon density matrices). We demonstrate the generation of high-dimensional maximally entangled photon pairs and show how the generated quantum state and its correlations can be controlled entirely optically using shaped pump fields interacting with the initially learned 3D NLPC structure—a feature that can find applications in qudit-based quantum key distribution and quantum information protocols that work at high switching rates. Our SPDCinv model has been made available at [83]. A preliminary short abstract of this work was presented at the CLEO 2021 conference [84]. Our use of the term "optimal" is indicative of *local optimality*, as is common in literature using deep learning and related techniques. We note in passing that there is an interesting vein of literature that aims to show that in the overparameterized context, locally optimal solutions are quite close to global optimality; see, for example [85,86], and references therein.

2. ALGORITHM DESIGN

A. Methodology

The procedure for the study of inverse problems in physical systems can be divided into the following three steps [7,87]: (i) identifying a minimal set of model parameters whose values completely characterize the system; (ii) identifying the physical laws and dynamics governing the system; and (iii) the use of actual results to infer the values of the model parameters. Given a desired observable set, $\mathbb{O}_d$, describing the quantum state or any related features, our goal is to find the unknown physical parameters, Λ, that characterize the system:

$$\Lambda = \boldsymbol{I}(\mathbb{O}_d), \tag{1}$$

where $\boldsymbol{I}(\cdot)$ is our inverse solver. We physically constrain our SPDCinv model by integrating it with the interaction dynamics of the SPDC process. In this manner, the model captures the interaction properties, such as diffraction, space-dependent nonlinear coupling, vacuum fluctuations, and non-perturbative effects. We consider SPDC in a bulk nonlinear crystal of uniform refractive index and spatially varying second-order nonlinearity, $\chi^{(2)}$. The dynamics is prescribed by the Heisenberg equations of motion:

$i\hbar\partial_t\hat{E} = [\hat{E}, \hat{H}_{\mathrm{SPDC}}]$, for the field operators $\hat{E}$ evolving under the SPDC Hamiltonian $\hat{H}_{\mathrm{SPDC}}$, where $\hbar$ is the reduced Planck's constant. To solve the dynamics, we transform the quantum Heisenberg equations of motion to the frequency domain and assume an undepleted continuous-wave pump field. We further take the slowly varying envelope approximation for the field operators and assume that the generated photons are post-selected using a narrow spectral filter, as extensively detailed in the Supplement 1, Section B [88]. These assumptions lead to dynamics in terms of a single longitudinal mode, i.e., for quasi-monochromatic photons, while allowing an arbitrary transverse spatial envelope and diffraction of each photon. It is worth noting that our model could be readily extended to include temporal walk-off and group-velocity dispersion effects (see Supplement 1, Section B.2). Decoherence due to linear absorption is also neglected, since absorption is typically small in the optical range [89,90]. Finally, we assume that photorefraction does not play a role, which is true for periodically poled KTP (PPKTP) and since the existing photorefraction of periodically poled lithium niobate (PPLN) can be mitigated either by Mg-doping, by working at high temperatures and/or at near-IR wavelengths.

Our model takes advantage of the common theoretical scenario in SPDC, where the initial state of the optical field is the vacuum state $|0\rangle$ and the interaction Hamiltonian is quadratic in the field operators. This enables us to expand the first- and second-order correlation functions—and, in principle, arbitrary-order correlations—of the resulting photonic state in terms of only single-photon amplitudes. Namely, the matrix elements of the correlation functions have the form $\langle 1|\hat{E}|0\rangle$ and $\langle 0|\hat{E}|1\rangle$ (see Supplement 1, Section B.1). By projecting the Heisenberg equations of motion onto these matrix elements, we obtain two pairs of c-number coupled wave equations along the 3D interaction medium [25], given as

$$i\frac{\partial E_i^{\mathrm{out}}}{\partial\zeta} = -\frac{\nabla_\perp^2}{2k_i}E_i^{\mathrm{out}} + \kappa_i e^{-i\Delta k\zeta}(E_s^{\mathrm{vac}})^*,$$

$$i\frac{\partial E_i^{\mathrm{vac}}}{\partial\zeta} = -\frac{\nabla_\perp^2}{2k_i}E_i^{\mathrm{vac}} + \kappa_i e^{-i\Delta k\zeta}(E_s^{\mathrm{out}})^*,$$

$$i\frac{\partial E_s^{\mathrm{out}}}{\partial\zeta} = -\frac{\nabla_\perp^2}{2k_s}E_s^{\mathrm{out}} + \kappa_s e^{-i\Delta k\zeta}(E_i^{\mathrm{vac}})^*,$$

$$i\frac{\partial E_s^{\mathrm{vac}}}{\partial\zeta} = -\frac{\nabla_\perp^2}{2k_s}E_s^{\mathrm{vac}} + \kappa_s e^{-i\Delta k\zeta}(E_i^{\mathrm{out}})^*, \tag{2}$$

where $\zeta = z$ is the coordinate along the direction of propagation. In the above equation, E_j^{out}, E_j^{vac} ($j = i, s$ for the idler and signal fields, respectively) are the "output" and "vacuum" field amplitudes, corresponding to the aforementioned matrix elements as $E_j^{\mathrm{out}} = \langle 1|\hat{E}_j|0\rangle$ and $E_j^{\mathrm{vac}} = \langle 0|\hat{E}_j|1\rangle$, where the single-photon state $|1\rangle$ can be arbitrary; $\nabla_\perp^2$ is the transverse Laplacian operator; k_j is the wavenumber; $\kappa_j(\mathbf{r},\zeta) = \frac{\omega_j^2}{c^2 k_j}\chi^{(2)}(\mathbf{r},\zeta)\mathcal{E}_p(\mathbf{r})$ is the nonlinear-coupling coefficient, where $\mathbf{r} = (x, y)$ is a position on the transverse plane; $\chi^{(2)}(\mathbf{r},\zeta)$ stands for the (spatially varying) second-order susceptibility, and $\mathcal{E}_p(\mathbf{r})$ is the (spatially varying) pump field envelope; c is the speed of light in vacuum; and $\Delta k = k_p - k_s - k_i$ is the phase mismatch. To solve the two pairs of c-number coupled wave equations, Eq. (2), we need to specify a boundary condition at $z = 0$. This in principle could be done separately for each of the transverse photonic modes in the system, which may become inefficient for a continuous set of modes. In Supplement 1, Section B.4, we show that a choice of Gaussian white noise, with a standard deviation matching the vacuum field uncertainty, recovers the desired quantum correlation observables when averaged over a large ensemble of noise realizations—without the necessity to scan over all possible modes. The quantum vacuum noise is therefore emulated by initializing a large number of instances of such Gaussian noise in both the idler and signal amplitudes, E_i^{vac} and E_s^{vac}, at $z = 0$. We summarize Eq. (2) in a compact fashion by denoting all of the fields as $E = (E_i^{\mathrm{out}}, E_i^{\mathrm{vac}}, E_s^{\mathrm{out}}, E_s^{\mathrm{vac}})$, and writing

$$i\frac{\partial E}{\partial\zeta} = \mathcal{L}(\Lambda)E, \tag{3}$$

where $\mathcal{L}$ is the operator given by the righthand side of Eq. (2), and Λ represents the list of physical parameters described in the previous exposition. In practice, we will be particularly interested in the pump field $\mathcal{E}_p$ and second-order susceptibility $\chi^{(2)}$, that is, $\Lambda = (\mathcal{E}_p(\cdot), \chi^{(2)}(\cdot))$, with all other parameters being taken as fixed. However, we note that the formulation that follows is general, and does not depend on the parameters of interest.

The model described herein is derived directly from the Heisenberg equations of motion, solving the dynamics in terms of the aforementioned single-photon matrix elements. These encapsulate the complete information of the quantum state in the case of conventional SPDC, and the desired normally ordered observables are directly obtained from them. On the other hand, phase-space methods, first applied in [91,92], sample the quasiprobability distribution, while solving a set of stochastic dynamical equations for the field quadratures. Though these approaches share common grounds with our model for solving SPDC, for example, in the use of random boundary conditions in the Wigner function method [19,21–24,93], their formulation is different. For example, the Wigner method detailed in [20] results in symmetrically ordered observables that then need to be recast onto normally ordered ones to obtain the desired observables. Despite these differences, we envision that the proposed optimization methodology for our stochastic model could—with some modification—be generalized to incorporate these phase-space methods for modeling quantum optics.

We integrate the fields along the direction of propagation according to Eq. (2), and solve the coupled wave equations for the large ensemble of quantum vacuum realizations in parallel. We use a time-unfolded version [94] of the SSF method [73,95] to solve for the propagation along the crystal. Then, we derive the second-order statistics to describe the resulting quantum state, an approach that was validated against experimental results, for several cases of shaped pump beams and structured crystals [20,25,57,74,75] (see also Section 3.A). This strategy facilitates differentiation back through the model and enables application of the latest optimization methods for learning its physical parameters, thereby overcoming issues related to the fundamentally stochastic nature of the model.

In what follows, we shall refer to the solution of Eq. (2) [or alternatively, Eq. (3)], together with the mapping onto a particular set of observables of interest, denoted as $\mathbb{O}$, as our *forward model*. In particular, we write

$$\mathbb{O} = \mathcal{F}\left\{\mathbb{E}\left[\mathcal{P}(\Lambda)\right]\right\}, \tag{4}$$

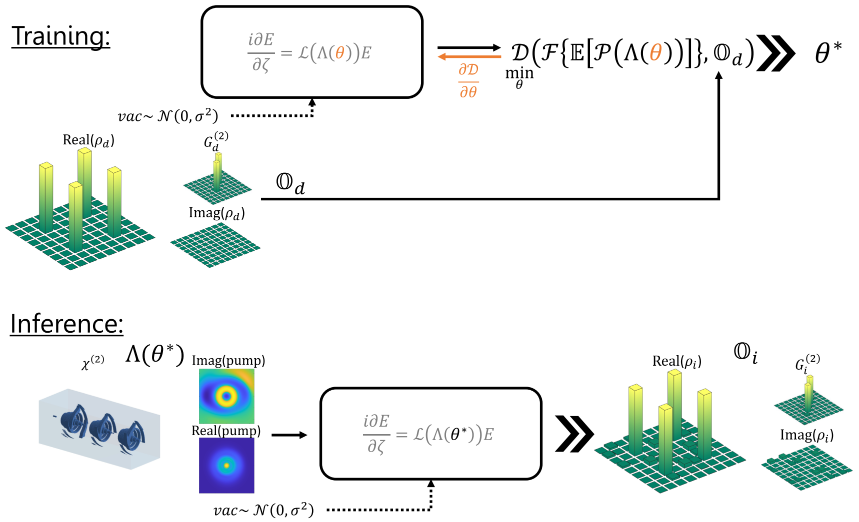

Fig. 2. Description of the SPDCinv algorithm in two phases. (1) In the training phase (upper panel), the parameterized version of the inverse design is solved. The model receives as input the desired observables and emits the parameterization of the physical parameters that will produce it, by solving the optimization problem. The learning process is described by applying gradient descent (in orange) to the appropriate discrepancy measure, $\mathcal{D}(\cdot, \cdot)$. (2) In the inference phase (lower panel), the model receives the computed physical parameters and emits the observables. The compact notation of the partial differential equation refers to the solution of the Heisenberg equations, Eq. (2). The quantum vacuum noise is integrated externally (dashed line).

where

- $\mathcal{P}(\Lambda)$ denotes the solution of Eq. (2) for the set of parameters Λ and a particular realization of vacuum noise, followed by projection of the output and noise fields onto a desired orthonormal basis;
- $\mathbb{E}$ denotes the expectation over vacuum noise, in practice achieved by computing the average over a large number of independent realizations of vacuum noise;
- operator $\mathcal{F}$ computes the first-order correlations that yield the desired observable (coincidence rate count, $G^{(2)}$, and density matrix of the bi-photon quantum state, ρ), as explained in greater detail in Section 2.B.

Given a desired observable set, $\mathbb{O}_d$, the general inverse problem involves finding the physical parameters Λ that produce it. We take a parameterized approach to solving the inverse problem. In particular, suppose that the physical parameters of interest Λ depend upon parameters θ that specify them, i.e., $\Lambda = \Lambda(\theta)$. Such parameters θ may, for example, be coefficients of basis expansions; we will see concrete examples shortly. In this case, we solve the inverse problem by solving the optimization problem

$$\theta^* = \min_{\theta} \ \mathcal{D}(\mathcal{F}\{\mathbb{E}[\mathcal{P}(\Lambda(\theta))]\}, \mathbb{O}_d). \tag{5}$$

In the above, $\mathcal{D}(\cdot, \cdot)$ is a discrepancy measure between two sets of observables. For example, we may take $\mathcal{D}(\mathbb{O}, \mathbb{O}') = \|\mathbb{O} - \mathbb{O}'\|_\beta$, where $\|\cdot\|_\beta$ is the Euclidean β-norm; alternatively, if the observables are normalized to unit 1-norm, then $\mathcal{D}$ can be the Kullback–Leibler divergence. In the case where we are measuring the discrepancy between two density matrices, we may take $\mathcal{D}$ to be the trace distance [96]. In Eq. (5), we are therefore trying to minimize the discrepancy between the set of observables given by a particular parameter specification θ, and the desired set of observables $\mathbb{O}_d$. The inverse model is then given by

$$\boldsymbol{I}(\mathbb{O}_d) = \Lambda(\theta^*). \tag{6}$$

To solve the optimization problem in Eq. (5), an approach based on gradient descent may be employed. The key is that the forward model of Eq. (2), while quite complicated, can be expressed in such a way that it is fully differentiable. As a result, any library that can auto-differentiate a system may be used to compute the relevant gradients, thereby allowing for the solution to the optimization problem in Eq. (5). In practice, we use JAX [97], a Python library designed for high-performance numerical computing and automatic differentiation.

Finally, given the solution to the inverse problem, we may run the forward model to compute the observables that actually result from the interaction parameters we have computed, that is,

$$\mathbb{O}_i = \mathcal{F}\left\{\mathbb{E}\left[\mathcal{P}(\Lambda(\theta^*))\right]\right\}, \tag{7}$$

where subscript i indicates *inference*. The degree to which the inferred observables $\mathbb{O}_i$ match the desired observables $\mathbb{O}_d$ will indicate the quality of the inverse algorithm. The overall algorithm is summarized in Fig. 2.

Interaction Parameters. We may learn any physical parameters Λ of the interaction, e.g., wavelength, temperature profile, poling period, poling profile, etc. In this work, the 2D/3D NLPC structure, $\chi^{(2)}(\mathbf{r}, \zeta)$, and pump beam profile, $\mathcal{E}_p(\mathbf{r})$, are the unknown physical parameters we seek to learn, that is, $\Lambda = (\mathcal{E}_p(\cdot), \chi^{(2)}(\cdot))$. We parameterize the 2D/3D NLPC structure and pump beam profile by multi-dimensional parameters $\theta_{\mathcal{E}}$ and θ_χ, respectively, such that $\Lambda(\theta) = (\mathcal{E}_p(\cdot; \theta_{\mathcal{E}}), \chi^{(2)}(\cdot; \theta_\chi))$. We now discuss in more detail how this parameterization is performed.

The parameters we learn can be as general as we want, subject to technological and physical restrictions. To decrease the dimensionality of learned parameters to ensure smoother convergence of the inverse problem's solution, the continuous functions of the NLPC structures are represented using a finite set of unknowns. One way to do this is through expansion in set basis functions that are mutually orthogonal, which may also change as a function of the propagation coordinate, ζ; the parameters θ then include the coefficients of the expansion. Examples include the Hermite–Gauss (HG) and Laguerre–Gauss (LG) bases, though many other possibilities exist. These basis functions are often scaled according to a transverse length, which for light beams is usually referred to as the waist size, a term we adopt hereafter for all basis functions. Learning the waist sizes of each of the basis functions individually adds further degrees of freedom to our model. The exact role of the parameters can be seen by formally writing the NLPC structure and the pump profile as a linear combination of the basis functions:

$$\chi^{(2)}(\mathbf{r},\zeta;\theta_\chi)=\sum_{n=1}^{N_\chi}\alpha_\chi^n\Phi_\chi^n(\mathbf{r},\zeta;w_\chi^n),\qquad \theta_\chi=\left\{\left(\alpha_\chi^n,w_\chi^n\right)\right\}_{n=1}^{N_\chi},$$

$$\mathcal{E}_p(\mathbf{r};\theta_\mathcal{E})=\sum_{n=1}^{N_\mathcal{E}}\alpha_\mathcal{E}^n\Phi_\mathcal{E}^n(\mathbf{r};w_\mathcal{E}^n),\qquad \theta_\mathcal{E}=\left\{\left(\alpha_\mathcal{E}^n,w_\mathcal{E}^n\right)\right\}_{n=1}^{N_\mathcal{E}},\tag{8}$$

where $\alpha_\chi^n,\alpha_\mathcal{E}^n$ are the learned basis coefficients; $w_\chi^n,w_\mathcal{E}^n$ are the learned basis function waist sizes; and $\Phi_\chi^n,\Phi_\mathcal{E}^n$ are the basis functions. Here, the basis function index n sums over both transverse modal numbers, for example, the orbital angular momentum (OAM) l- and radial p-indices for LG modes.

B. Observables

The set of desired observables describing the generated quantum state is given by the coincidence rate count, $G^{(2)}$, and density matrix of the bi-photon quantum state, ρ, such that in general, $\mathbb{O}_d=(G_d^{(2)},\rho_d)$. Their evaluation is achieved by first solving Eq. (2) over a large number of independent realizations of vacuum noise, projecting the output and noise fields onto a desired orthonormal basis of optical modes, and then taking the ensemble average to obtain first-order correlations [20,25] (see also Supplement 1, Section B), which (for the signal) is given by $G^{(1)}(q_s,q_s')=\langle\psi|a_{q_s}^\dagger a_{q_s'}|\psi\rangle$. Here, $|\psi\rangle$ denotes the quantum state, $a(a^\dagger)$ denotes the photon annihilation (creation) operator, and q_s denotes any quantum number of the signal photon, for example, LG modes, HG modes, etc. Second-order correlations are derived using the fact that the quantum state of SPDC, the squeezed vacuum state [98], belongs to the family of Gaussian states, for which all higher-order correlations can be obtained from the first-order ones [99] (Supplement 1, Section B.6). The coincidence rate is given by the second-order quantum correlation function, which determines the probability of finding an idler photon in mode q_i and a signal photon in mode q_s:

$$G^{(2)}(q_i,q_s,q_s,q_i)=\langle\psi|a_{q_i}^\dagger a_{q_s}^\dagger a_{q_s}a_{q_i}|\psi\rangle.\tag{9}$$

To extract the optimal model parameters that generate the desired quantum correlations over a given basis, we solve the optimization problem in Eq. (5). Here, $\mathcal{D}(\cdot,\cdot)$ is taken as a typical measure of discrepancy between two probability distributions. For example, we may use the Kullback–Leibler divergence [100], the L1 norm [101], or an ensemble of both.

To obtain the full quantum state generated by the SPDC process, we use QST [102–104]. Equation (9) allows for the calculation of any coincidence measurement performed on the system, on any basis of our choice. Since the process of QST involves a sequence of projective coincidence measurements on different bases, we can readily reconstruct the density matrix, ρ, of the entangled two-qudit state through a series of linear operations. Here, naturally, $\mathcal{D}(\cdot,\cdot)$ [in Eq. (5)] is taken to be the trace distance [96]—a metric on the space of density matrices that measures the distinguishability between two states.

The tomographic reconstruction is performed using the correlation data collected from the projections of the simulated bi-photon state onto orthogonal as well as mutually unbiased bases (MUBs) [103,104]. The density matrix of the bi-photon system can be written as

$$\rho=\frac{1}{d^2}\sum_{m,n=0}^{d^2-1}\rho_{mn}\sigma_m\otimes\sigma_n,\tag{10}$$

where σ_m is the set of generators that span the d-dimensional tomography space (for example, Pauli and Gell-Mann matrices for $d=2$ and 3, respectively). The expansion coefficients ρ_{mn} are found via

$$\rho_{mn}=\sum_{i,j=0}^{d-1}a_m^i a_n^j\langle\lambda_m^i\lambda_n^j|\rho|\lambda_m^i\lambda_n^j\rangle,\tag{11}$$

with a_m^i and $|\lambda_m^i\rangle$ denoting the ith eigenvalue and eigenstate of σ_m, respectively [104]. The required projections inside the sum function are found in a manner similar to Eq. (9), with the pure basis states replaced by the MUBs, when necessary.

3. RESULTS

The proposed method can be readily employed to generate desired quantum correlations between SPDC structured photon pairs. Further, by emulating QST integrated into the learning stage, we can tailor specific, high-dimensional quantum states desirable for photonic quantum information and communication. In this section, we use our algorithm to solve the inverse design problem and extract the optimal 2D or 3D NLPC structure and the complex pump beam structures for generating desired second-order quantum correlations or density matrices. We let our algorithm learn the NLPC structures, the complex pump beam profiles, or both. We discover that the quantum state of SPDC photons and their correlations can be all-optically controlled by first learning the crystal structure with a given pump mode, and then changing the initial pump mode in inference phase. This active optical control has the advantage of altering the quantum state in a non-trivial manner, while retaining its purity. Further, we find that learning the crystal structure and the pump beam profile simultaneously can improve the accuracy of the generated results, in comparison with the desired state. The SPDCinv training phase takes about 1 h on four NVIDIA T4 16 gb GPUs, for all configurations involving 1 mm long NLPCs.

A. Model Validation

Before we delve into inverse design problems, we first validate our model against published experimental results of SPDC shaping [57,59]. This comes in addition to the multiple, already presented, validations of our model [25]. Figure 3 presents the use of our model for recovering the experimental results reported by Kovlakov *et al.* [59]. We reproduce the coincidence rate counts for a qutrit state, Fig. 3(a), and ququint state, Fig. 3(b), in the LG basis, generated by a shaped pump field. We restrict the shaped pump field to the same modes reported in [59]. To show the capability of

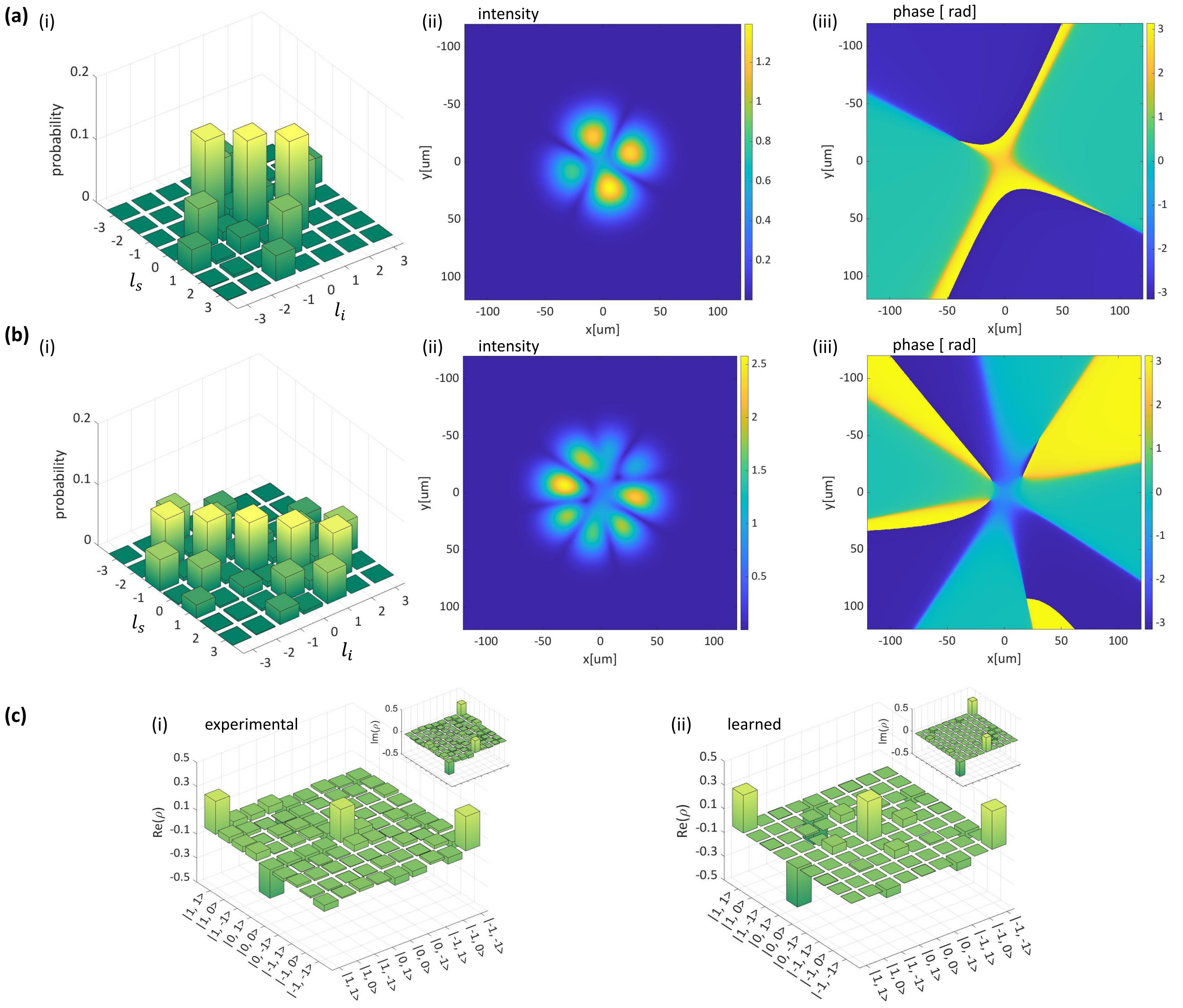

Fig. 3. Model validation against experimental results reported by Kovlakov *et al.* [59]. (a) LG qutrit state: SPDCinv model generated coincidence rate counts (i), and the corresponding pump intensity (ii) and phase (iii). (b) LG ququint state: SPDCinv model generated coincidence rate counts (i), and the corresponding pump intensity (ii) and phase (iii). (c) LG qutrit density matrix: experimental result [59] (i) and SPDCinv model generated result (ii).

our model to simulate the QST procedure, we recover the density matrix of the qutrit state, Fig. 3(c), as reported by Kovlakov *et al.* [59]. The resulting quantum states, coincidence rate counts, and pump fields (used to recover the result in inference) are in good agreement with experiments (deviations may arise from detection, OAM projection, and coupling imperfections, as acknowledged by Kovlakov *et al.* [59]). To demonstrate the model agreement, we calculate the mean squared error (MSE) values of the learned coincidence rate counts, the corresponding pump field coefficient amplitudes, and the density matrix against experimental results. For qutrit coincidence rate counts, we obtain MSE of 4.11×10^{-5} [Fig. 3(a)(i)], and for ququint coincidence rate counts, we obtain MSE of 8.76×10^{-5} [Fig. 3(b)(i)]. For the matching pump field coefficient amplitudes, we obtain MSEs of 1.59×10^{-2} and 1.92×10^{-2}, respectively. For the qutrit density matrix, the MSE is 4.60×10^{-3} [Fig. 3(c)]. We provide additional comparisons in tabular form in Supplement 1, Section A.4, Tables 1–4. Next, we follow another result reported by Kovlakov *et al.* [57] and let our algorithm learn the optimal pump waist size for generating a pure HG spatial Bell state between structured SPDC photon pairs. Figure 4 shows the convergence of our learning algorithm towards the optimal pump waist, $w_p = \sqrt{L/k_p}$ [57], for the case of $L = 5$ mm. As the learning process progresses, the discrepancy measure, $\mathcal{D}(\cdot,\cdot)$ Eq. (5), reduces until the model reaches convergence. Accordingly, the size of the pump waist converges to the required value [57], and a clear Bell state, $(|0, 1\rangle + \exp(i\phi)|1, 0\rangle)/\sqrt{2}$, is generated.

B. Shaping Arbitrary Quantum Correlations

First, we let our algorithm learn the physical parameters for desired quantum correlations—that is, the two-photon coincidence rate counts—between structured SPDC photon pairs. The learned parameters are the spatial modes of the NLPC structure and pump structure, according to Eq. (8). We use a type-2 SPDC process in a 1 mm long KTP NLPC, quasi-phase-matched to on-axis generation of photon pairs at 810 nm from a 405 nm pump wave. We

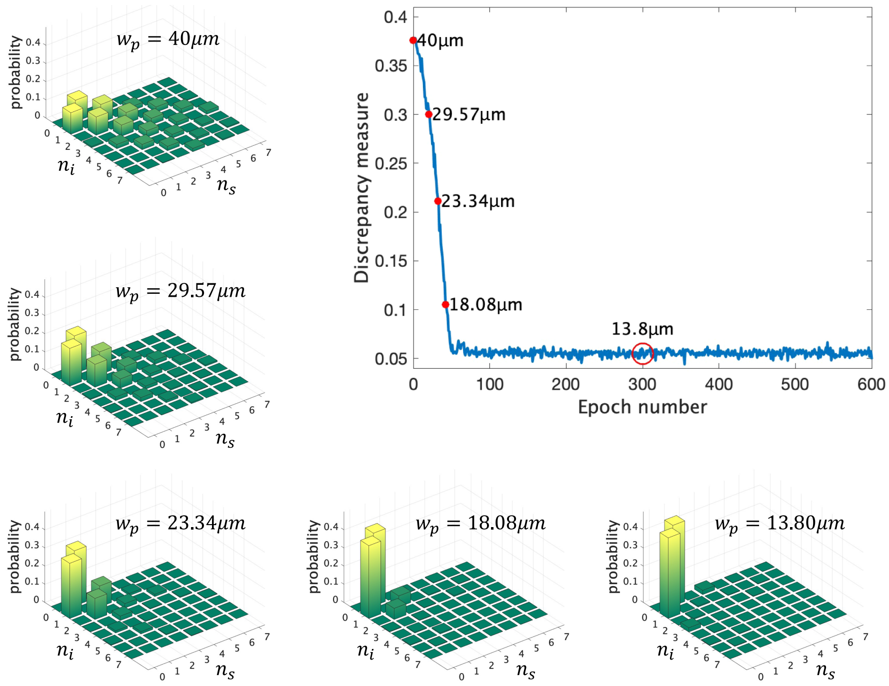

Fig. 4. Model validation against experimental results reported by Kovlakov *et al*. [57] for shaped correlations corresponding to the Bell state $(|0,1\rangle + \exp(i\phi)|1,0\rangle)/\sqrt{2}$. The upper-right figure is the discrepancy measure [Eq. (5)] between the generated coincidence rate counts and the desired one [57] versus training epoch number. The only learned physical parameter is the pump waist, and we let our algorithm find its optimal value for generating the desired quantum correlations. We sample the obtained pump waist along the discrepancy curve (red dots and insets) to see the evolution of the generated coincidence count rates under the optimized pump waist. At convergence, the algorithm obtains the correct pump waist value of $w_p = \sqrt{L/k_p} \approx 13.8$ µm for $L = 5$ mm for generating a pure HG Bell state.

---

assume that the pump beam is linearly polarized along the y direction and that the $\chi^{(2)}$ nonlinear coefficient can attain one of two binary values of $+d_{24}$ and $-d_{24}$. We project the generated photons on either LG modes with integer quantum numbers l, p, standing for the azimuthal and radial numbers, respectively, or HG modes, with integer quantum numbers n, m, standing for x- an y-axis mode numbers, respectively. When considering the coincidence rate counts, we post-select either the radial index ($p = 0$), in the case of the LG basis, or the y-axis modal number ($m = 0$), in the case of the HG basis. The discrepancy measure in Eq. (5) is taken as a weighted ensemble of the Kullback-Leibler divergence and the L1 norm.

Laguerre–Gauss Basis. Here, we show all-optically coherent control over quantum correlations of SPDC photons, in the LG basis (Fig. 5 depicts the results of this section). We use our algorithm to extract the optimal 3D NLPC structures for generating the desired coincidence rate counts of maximally entangled two-photon qubit $|\psi\rangle = (|1,-1\rangle + \exp(i\phi)|-1,1\rangle)/\sqrt{2}$ and ququart $|\psi\rangle = (|-2,1\rangle + \exp(i\phi_1)|0,-1\rangle + \exp(i\phi_2)|-1,0\rangle + \exp(i\phi_3)|1,-2\rangle)/\sqrt{4}$ states, which can later be actively controlled via the pump beam (the indices of the signal and idler photons are the azimuthal indices). We start by letting the algorithm learn the optimal 3D NLPC structure with a constant Gaussian pump beam, presented in Figs. 5(a)(iv), 5(a)(v) and 5(b)(iv), 5(b)(v). The obtained 3D NLPC [Figs. 5(a)–5(b)(v)] display an intricate structure: concentric rings, Fig. 5(a)(v), which mark the coupling to radial LG modes ($p > 0$), and corkscrew structures, Fig. 5(b)(v), indicating an intrinsic chirality of the 3D NLPC structure. We find that the coupling to radial modes is essential for quantum destructive and constructive interference in the post-selected subspace ($p = 0$), while the crystal-handedness is responsible for inducing OAM. The generated quantum correlations coincide remarkably well with the target, Figs. 5(a)(i), 5(a)(ii) and 5(b)(i), 5(b)(ii), with MSE of 6.24×10^{-5} for qubit state and 5.02×10^{-5} for ququart state (a tabular comparison is provided in Supplement 1, Section A.4, Tables 5 and 6).

The learned crystal structures demonstrate an even richer functionality—they can span a larger variety of output correlations when the input pump mode is altered from Gaussian ($l = 0$) to other LG modes, as depicted in Figs. 5(a)–5(b)(vi). As we alter the initial pump mode, the new correlations differ significantly from those obtained in the original design, while they still correspond to maximally entangled states. Moreover, the new correlations keep the high signal to noise ratio (SNR) between the primary two-photon modes and the background of the coincidence signal, as can be seen in Figs. 5(a)–5(b)(iii). For example, by introducing an external pump OAM, a qubit state originally on the $l_i + l_s = 0$ diagonal is shifted to a qubit on the $l_i + l_s = 1$ diagonal, Fig. 5(a), when $l_p = 1$. Similarly, a ququart on the $l_i + l_s = -1$ diagonal is shifted to the $l_i + l_s = 1$ diagonal when $l_p = 2$, Fig. 5(b). Interestingly, by using other learned crystal structures and superpositions of LG modes in the pump beam, we discover nontrivial pump-induced transformations, between a qutrit and a ququart, and a ququart and a qubit (see Supplement 1, Section A.1, Fig. A.1).

Hermite–Gauss Basis. In the previous example, in the LG basis, the learning step was performed by varying only the crystal parameter. Now, we show that by learning the crystal structure and the pump beam profile simultaneously, we can improve the quality of the generated second-order quantum correlations.

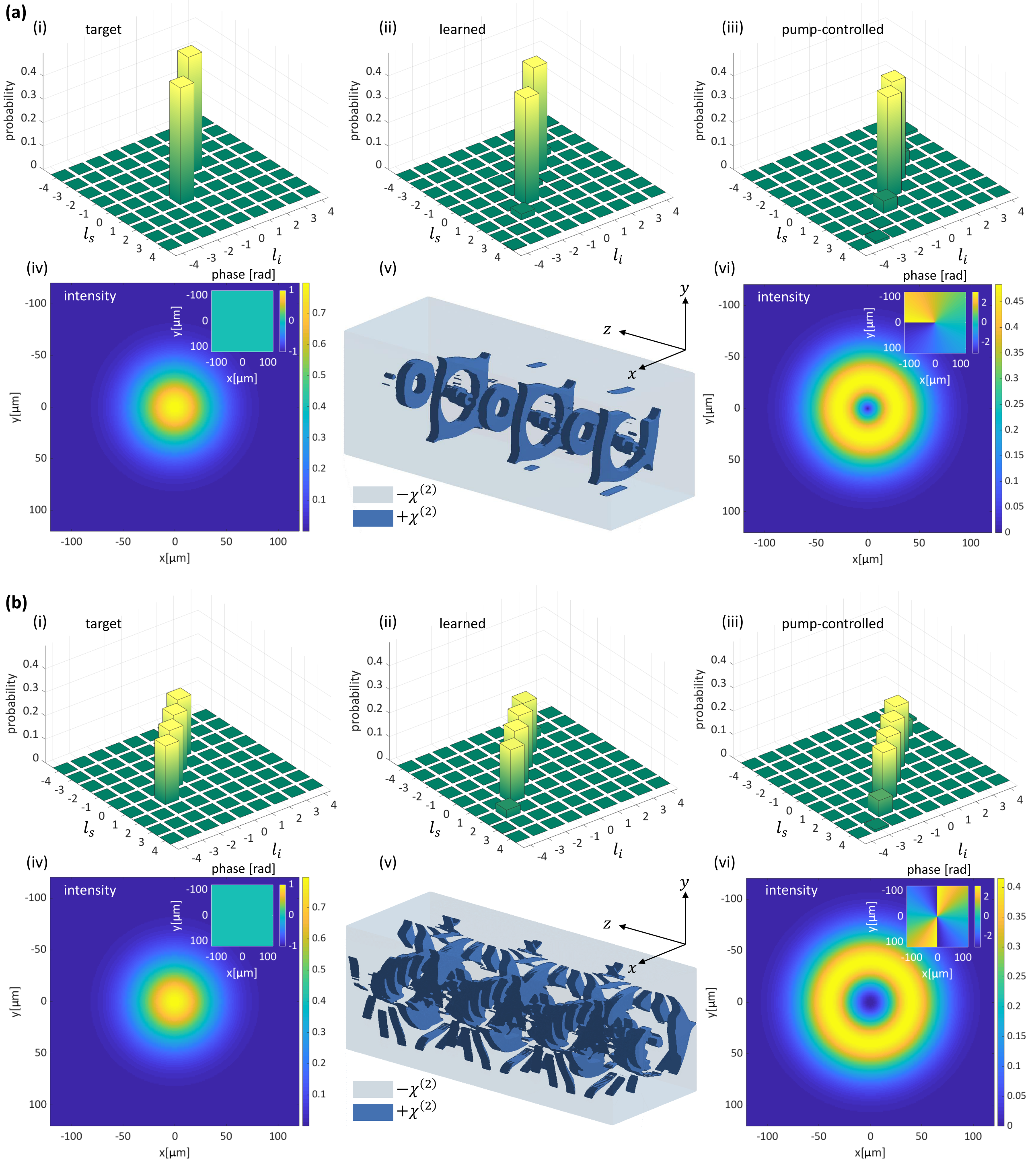

Fig. 5. Inverse design and all-optical coherent control over quantum correlations of SPDC photons: maximally entangled two-photon states in the LG basis. (a) Shaped correlations corresponding to the qubit state $|\psi\rangle = (|1, -1\rangle + \exp(i\phi)|-1, 1\rangle)/\sqrt{2}$. (i) Target coincidence probability; (ii) learned coincidence probability, for an initial Gaussian pump (iv) and the learned 3D NLPC structure (v). In (v), three successive unit cells are shown (the z axis is scaled-up by a factor of 20). All-optical control over the coincidence probability is demonstrated using a LG_{01} pump mode (vi), with the same learned crystal, giving quantum correlations that correspond to a new qubit state, $|\psi\rangle = (|0, 1\rangle + \exp(i\phi)|1, 0\rangle)/\sqrt{2}$ (iii). (b) Shaped correlations corresponding to the ququart state $|\psi\rangle = (|-2, 1\rangle + \exp(i\phi_1)|0, -1\rangle + \exp(i\phi_2)|-1, 0\rangle + \exp(i\phi_3)|1, -2\rangle)/\sqrt{4}$. (i)–(v) As in (a). All-optical control over the coincidence probability is demonstrated using a LG_{02} pump mode (vi), with the same learned crystal, giving quantum correlations that correspond to a different ququart state, residing on the $l_i + l_s = +1$ diagonal, $|\psi\rangle = (|2, -1\rangle + \exp(i\phi_1)|0, 1\rangle + \exp(i\phi_2)|1, 0\rangle + \exp(i\phi_3)|-1, 2\rangle)/\sqrt{4}$ (iii).

In this section, we explore the photon correlations in the HG basis and our target is a two-photon ququart state: $|\psi\rangle = (|0, 1\rangle + \exp(i\phi_1)|1, 0\rangle + \exp(i\phi_2)|1, 2\rangle + \exp(i\phi_3)|2, 1\rangle)/\sqrt{4}$ (the indices of the signal and idler photons are the HG modes indices in the y direction). We consider designs that use more mature NLPC technologies, such as electric field poling [105], which are

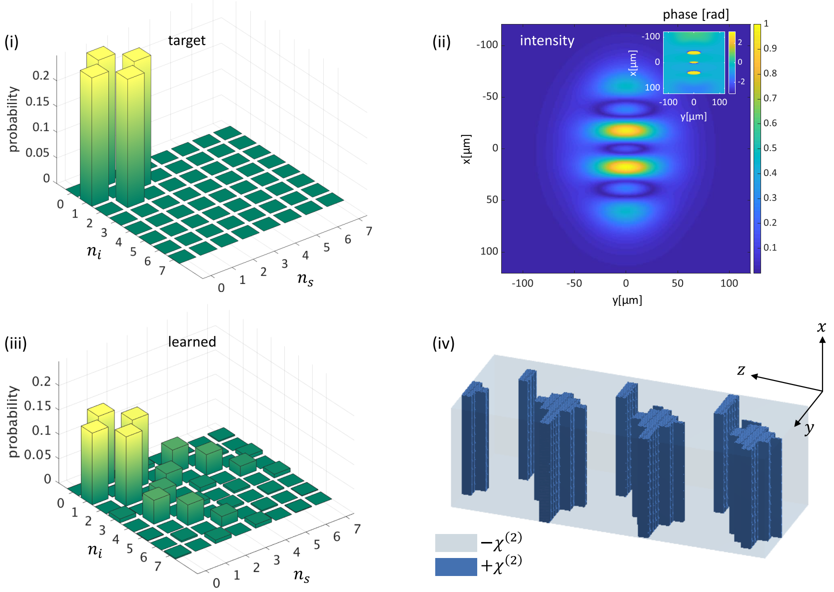

Fig. 6. Inverse design of quantum correlations of SPDC photons: maximally entangled two-photon states in the HG basis. Shaped correlations corresponding to the ququart state $|\psi\rangle = (|0, 1\rangle + \exp(i\phi_1)|1, 0\rangle + \exp(i\phi_2)|1, 2\rangle + \exp(i\phi_3)|2, 1\rangle)/\sqrt{4}$. (i) (ii) Respectively, target and learned coincidence rate counts. (iii), (iv) Simultaneously learned 2D NLPC structure and complex pump beam profile, restricted to vary only in the x direction. In (iii), three successive unit cells are shown (the z axis is scaled-up by a factor of 20).

restricted to 2D nonlinear crystal structures. We use our algorithm to simultaneously extract the optimal 2D NLPC structure that varies only in the y direction and the pump beam profile that is restricted to varying only in the x direction, for generating the desired coincidence rate counts of a maximally entangled two-photon ququart. In Fig. 6(ii), we see the generated coincidence rate counts that result from the computed interaction parameters. While the probabilities of the generated ququart state are lower than the desired target, they are equal to and significantly larger than other unwanted probabilities. This result is certainly exciting when taking into account the restrictions we considered under 2D variation. The obtained crystal structure [Fig. 6(iii)] and the pump profile [Fig. 6(iv)] display a Cartesian structure.

To better show the importance of combining both the crystal structure and the pump beam profile to obtain the desired maximally entangled state, we compared the quality of the generated second-order quantum correlations of a ququart state under the following three scenarios: using our algorithm to solve the inverse design problem and (1) extracting the optimal 3D NLPC structure with a constant Gaussian pump; (2) extracting the complex pump beam profile, with a constant periodically poled crystal; and (3) extracting both the optimal 3D NLPC structure and the optimal complex pump beam profile. The simultaneous learning of the pump and crystal clearly outperforms the individual learning of either. This is attributed to higher modes created by the multiplication of modes composing the pump and crystal structure in the nonlinear coupling coefficient, κ_j [in Eq. (2)]. Also, there seemed to be no preference in the generated results while optimizing separately either the NLPC or the pump, which shows the similar role of each of them in the nonlinear coupling coefficient. For visual results, see Supplement 1, Section A.2, Fig. A.2.

C. Shaping Arbitrary Quantum States

To resolve a specific two-photon quantum state generated by the tailored SPDC process, a coincidence measurement will not suffice. For this purpose, we emulate QST and integrate it into our learning stage for evaluating the corresponding density matrix, as detailed in Section 2.2. The density matrix is used as an observable, while the trace distance is taken as the discrepancy metric $\mathcal{D}(\cdot, \cdot)$ [Eq. (5)]. As a proof of concept, we consider two-photon qudit states with dimension $d = 3$ in the LG basis. That is, we focus on the subspace spanned by $\{|-1\rangle, |0\rangle, |1\rangle\} \otimes \{|-1\rangle, |0\rangle, |1\rangle\}$, giving a 9×9 dimensional density matrix.

Similar to the previous subsection, we use our algorithm to simultaneously extract the optimal 3D NLPC structures and the pump beam profiles, for generating the desired quantum states. Figure 7(a) depicts the results for the maximally entangled state $|\psi\rangle = (|1, -1\rangle + |-1, 1\rangle)/\sqrt{2}$ [corresponding to the coincidence rate shown in Fig. 5(a)(i)], while Fig. 7(b) depicts the results for the maximally entangled state $|\psi\rangle = (|1, -1\rangle + |0, 0\rangle + |-1, 1\rangle)/\sqrt{3}$ (corresponding to the coincidence rate shown in Supplement 1, Fig. A.1(a)(i)). The generated density matrices fit the target states well, as evident in Figs. 7(a)(i), 7(a)(iii) and 7(b)(i), 7(b)(iii), with MSE of 4.51×10^{-4} for qubit state and 1.87×10^{-4} for qutrit state (a tabular comparison is provided in Supplement 1, Section A.4, Tables 7 and 8). Our learned pump profiles and crystal structures demonstrate concentric shapes, Figs. 7(a)(ii), 7(a)(iv) and 7(b)(ii), 7(b)(iv). These maintain a total OAM of $l_i + l_s = 0$, as expected, while making higher-order radial LG modes possible. These higher-order modes are responsible, for example, for removing the two-photon Gaussian mode $|00\rangle$ in the first learned state, Figs. 7(a)(i) and 5(a)(ii), through destructive interference, which is otherwise impossible when using only Gaussian pump beams.

Importantly, the generated quantum two-photon states are sensitive to the relative phase between the modes constructing

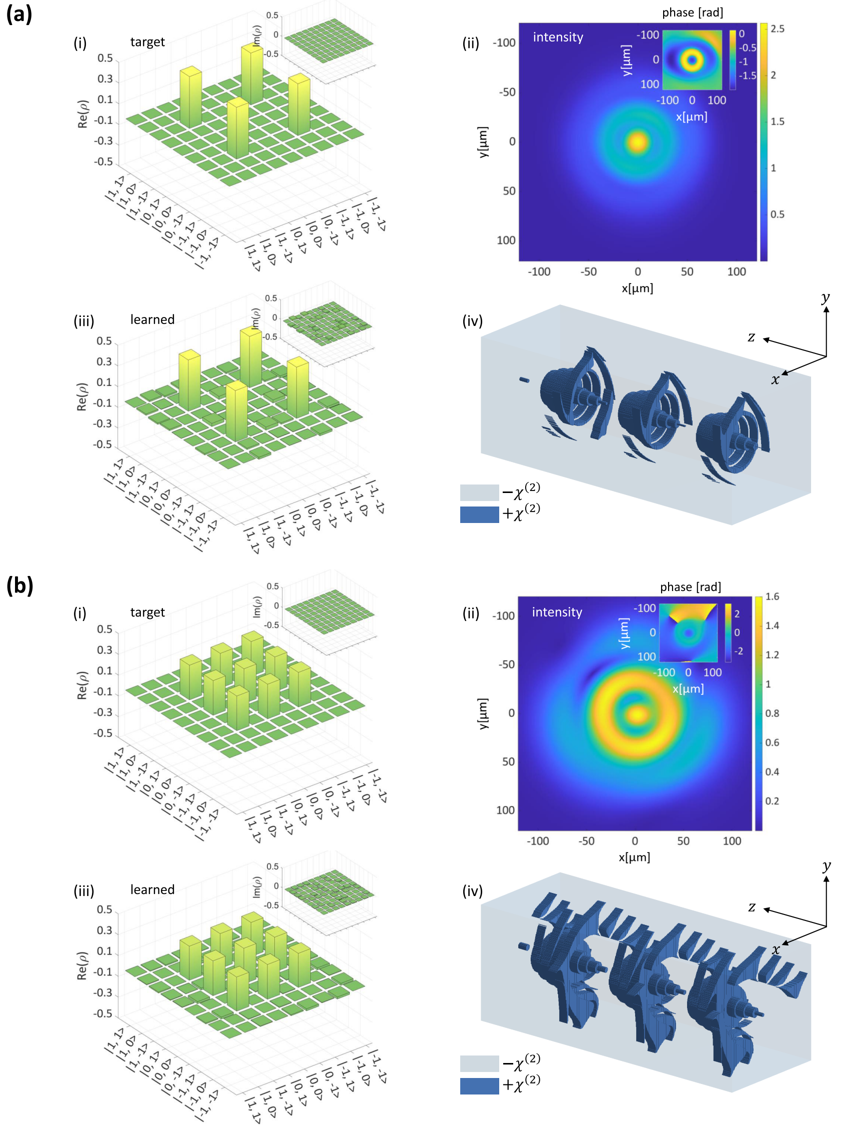

Fig. 7. Inverse design of quantum state density matrices of SPDC photons: maximally entangled two-photon states in the LG basis. (a) Qubit state $|\psi\rangle = (|1,-1\rangle + |-1,1\rangle)/\sqrt{2}$. (i), (iii) Respectively, target and learned states (the real part of the density matrix is shown in large, and the imaginary in small). (ii), (iv) Simultaneously learned complex pump beam profile and 3D NLPC structure. In (iv), three successive unit cells are shown (the *z* axis is scaled-up by a factor of 20). (b) Qutrit state $|\psi\rangle = (|1,-1\rangle + |0,0\rangle + |-1,1\rangle)/\sqrt{3}$. (i)–(iv) As in (a).

the pump profile and the learned nonlinear crystal structure. This feature is essential for asserting that the active all-optical control over the coincidence rate counts, discussed in the previous section, allows also for quantum coherent control over the generated photon qudits. To demonstrate this, we again learn a 3D crystal structure with a fixed pump profile, but this time consisting of a given superposition of LG modes. By changing the relative phase between the LG modes, we expect that the off-diagonal terms in the density matrix change accordingly.

Figure 8 depicts the results for the generated maximally entangled two-photon ququart state $|\psi\rangle = (|-1,0\rangle + |0,-1\rangle + |1,0\rangle + |0,1\rangle)/\sqrt{4}$. Initially, we use our algorithm to extract the optimal 3D NLPC structure with a fixed pump beam of the form $\mathrm{LG}_{01} + e^{i\alpha}\mathrm{LG}_{0-1}$ for $\alpha = 0°$ [i.e., a HG_{10} mode, as presented in Fig. 8(a)(iii)]. The real part of the generated density matrix is shown in Figs. 8(a)(i) and the imaginary part in Fig. 8(a)(ii). The generated density matrix fits the desired one. We then used the extracted crystal structure with different superpositions of LG modes of the pump. Figures 8(b)(i), 8(b)(ii) and 8(c)(i), 8(cii) show the quantum states achieved through inference with the same learned crystal structure, but with the pump mode superposition phase angle α changed to $\alpha = 120°$, Fig. 8(b)(iii), and 240°, Fig. 8(c)(iii). This corresponds experimentally to a rotation of the HG_{10} mode. Note the significant change in the imaginary off-diagonal density matrix elements in Figs. 8(b)(ii) and 8(c)(ii). This indicates the coherent control over the quantum state via the rotation of the pump beam—a diverse functionality available by use of a single crystal structure pumped with different optical modes.

4. CONCLUSION

We have introduced an algorithm that yields promising results in the inverse design problem of generating structured and entangled

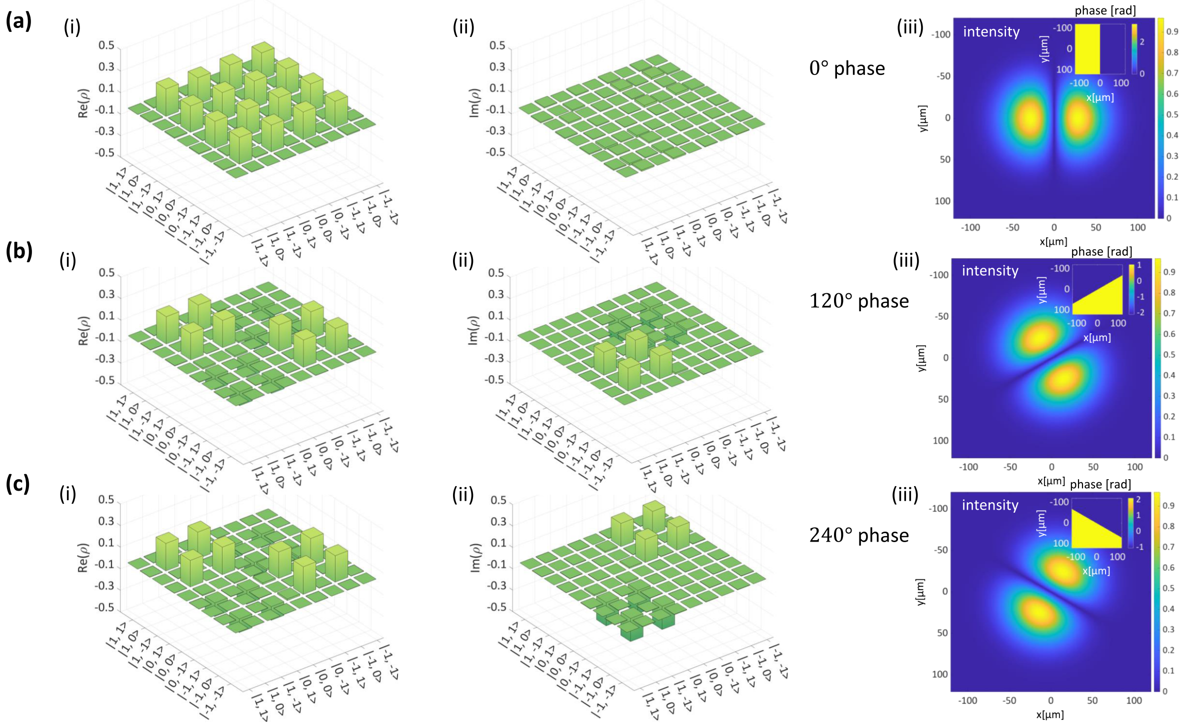

Fig. 8. Inverse design and all-optical coherent control over quantum state of SPDC photons: maximally entangled two-photon ququart state in the LG basis. We use our algorithm to extract the 3D NLPC structure that generates the desired ququart state $|\psi\rangle = (|-1, 0\rangle + |0, -1\rangle + |1, 0\rangle + |0, 1\rangle)/\sqrt{4}$, using the initial constant pump profile $\mathrm{HG}_{10} = \mathrm{LG}_{01} + \mathrm{LG}_{0-1}$ (a)(iii). The real part of generated density matrix is shown in (a)(i) and the imaginary part in (a)(ii). Next, the pump beam illuminating the learned crystal structure is rotated to actively control the generated quantum state. (b)(i), (ii) Real and imaginary parts, respectively, of generated density matrix for the rotated incident beam $\mathrm{LG}_{01} + e^{i120^\circ}\mathrm{LG}_{0-1}$ (b)(iii). (c)(i), (ii) Real and imaginary parts, respectively, of generated density matrix for the rotated incident beam $\mathrm{LG}_{01} + e^{i240^\circ}\mathrm{LG}_{0-1}$ (c)(iii).

photon pairs in quantum optics, using tailored nonlinear interactions in the SPDC process. The SPDCinv algorithm extracts the optimal physical parameters that yield a desired quantum state or correlations between structured photon pairs that can then be used in future experiments. To ensure convergence to realizable results and to improve the predictive accuracy, our algorithm obeyed physical constraints through the integration of the time-unfolded propagation dynamics governing the interaction of the SPDC Hamiltonian. We have shown how we can apply our algorithm to obtain the optimal nonlinear $\chi^{(2)}$ structures (2D/3D) as well as different pump structures for generating the desired maximally entangled states. The optimal NLPC structures extracted by our model seem to exhibit robustness against imperfections. To mimic crystal fabrication imperfections, we deliberately add errors to the crystal structure to impair the generated coincidence rate counts of the maximally entangled two-photon qubit. Then, we show how with a slight variation in a different parameter of the system (pump waist), we can divert the system back, to nearly recover the original system results (see Supplement 1, Section A.3). The high dimensionality of these generated states increases the bandwidth of quantum information, and can improve the security of quantum key distribution protocols [106,107]. We further demonstrate all-optical coherent control over the generated quantum states by actively changing the profile of the pump beam, making our results appealing for a variety of quantum information applications that require fast switching rates.

This work can readily be extended to the spectral–temporal domain, by allowing non-periodic crystal structures along the propagation axis—making it possible to shape the joint spectral amplitude [108] of the photon pairs. Furthermore, one can adopt our approach for other optical systems, such as nonlinear waveguides and resonators [109], $\chi^{(3)}$ effects (e.g., spontaneous four wave mixing [110]), spatial solitons [111,112], fiber optics communication systems [113,114], and even higher-order coincidence probabilities by increasing the pump intensity [115]. Moreover, the algorithm can be upgraded to include passive optical elements such as beam splitters, holograms, and mode sorters [8], thereby providing greater flexibility for generating and manipulating quantum optical states.

Looking to the future, several research directions may be considered. For instance, one may incorporate various decoherence mechanisms that result from losses such as absorption and scattering. Alternatively, our current scheme may be adapted to other quantum systems sharing a similar Hamiltonian structure, such as superfluids and superconductors [116]. In light of all this, we believe that this work, along with its complementary code (see Code 1, Ref. [83]), can contribute to further exciting advancements and discoveries in other quantum and classical systems.

Funding. Israel Science Foundation (1415/17); Ministry of Science, Technology and Space; The Israel Innovation Authority and the Tel Aviv University Center for Quantum Science and Technology.

Acknowledgment. We thank Google Cloud for supporting this work by giving us access to high computing power, as part of its Academic Research Grant. A.K. is supported by the Adams Fellowship of the Israeli Academy of Science and Humanities. We thank Dr. E.V. Kovlakov and Dr. S.P. Kulik for providing the experimental data that we use to evaluate our model. We acknowledge the Ministry of Science, Technology and Innovation, in the framework of India-Israel Bi-national Program; and the Innovation Authority, in the framework of the Quantum Communication Consortium.

Disclosures. The authors declare no conflicts of interest.

Data availability. Data underlying the results presented in this paper are available in [83].

Supplemental document. See Supplement 1 for supporting content.

REFERENCES

1. G. Carleo and M. Troyer, “Solving the quantum many-body problem with artificial neural networks,” Science **355**, 602–606 (2017).
2. M. Raissi, P. Perdikaris, and G. E. Karniadakis, “Physics-informed neural networks: a deep learning framework for solving forward and inverse problems involving nonlinear partial differential equations,” J. Comput. Phys. **378**, 686–707 (2019).
3. R. Iten, T. Metger, H. Wilming, L. Del Rio, and R. Renner, “Discovering physical concepts with neural networks,” Phys. Rev. Lett. **124**, 010508 (2020).
4. K. Choo, A. Mezzacapo, and G. Carleo, “Fermionic neural-network states for ab-initio electronic structure,” Nat. Commun. **11**, 2368 (2020).
5. A. A. Gentile, B. Flynn, S. Knauer, N. Wiebe, S. Paesani, C. E. Granade, J. G. Rarity, R. Santagati, and A. Laing, “Learning models of quantum systems from experiments,” Nat. Phys. **17**, 837–843 (2021).
6. G. E. Karniadakis, I. G. Kevrekidis, L. Lu, P. Perdikaris, S. Wang, and L. Yang, “Physics-informed machine learning,” Nat. Rev. Phys. **3**, 422–440 (2021).
7. A. Tarantola, *Inverse Problem Theory and Methods for Model Parameter Estimation* (SIAM, 2005).
8. M. Krenn, M. Malik, R. Fickler, R. Lapkiewicz, and A. Zeilinger, “Automated search for new quantum experiments,” Phys. Rev. Lett. **116**, 090405 (2016).
9. A. A. Melnikov, H. P. Nautrup, M. Krenn, V. Dunjko, M. Tiersch, A. Zeilinger, and H. J. Briegel, “Active learning machine learns to create new quantum experiments,” Proc. Natl. Acad. Sci. USA **115**, 1221–1226 (2018).
10. T. Tamayo-Mendoza, C. Kreisbeck, R. Lindh, and A. Aspuru-Guzik, “Automatic differentiation in quantum chemistry with applications to fully variational Hartree–Fock,” ACS Central Sci. **4**, 559–566 (2018).
11. I. Malkiel, M. Mrejen, A. Nagler, U. Arieli, L. Wolf, and H. Suchowski, “Plasmonic nanostructure design and characterization via deep learning,” Light Sci. Appl. **7**, 60 (2018).
12. S. Molesky, Z. Lin, A. Y. Piggott, W. Jin, J. Vucković, and A. W. Rodriguez, “Inverse design in nanophotonics,” Nat. Photonics **12**, 659–670 (2018).
13. K. Yao, R. Unni, and Y. Zheng, “Intelligent nanophotonics: merging photonics and artificial intelligence at the nanoscale,” Nanophotonics **8**, 339–366 (2019).
14. M. Minkov, I. A. Williamson, L. C. Andreani, D. Gerace, B. Lou, A. Y. Song, T. W. Hughes, and S. Fan, “Inverse design of photonic crystals through automatic differentiation,” ACS Photon. **7**, 1729–1741 (2020).
15. A. D. Jagtap, E. Kharazmi, and G. E. Karniadakis, “Conservative physics-informed neural networks on discrete domains for conservation laws: applications to forward and inverse problems,” Comput. Methods Appl. Mecha. Eng. **365**, 113028 (2020).
16. M. Krenn, M. Erhard, and A. Zeilinger, “Computer-inspired quantum experiments,” Nat. Rev. Phys. **2**, 649–661 (2020).
17. S. Colburn and A. Majumdar, “Inverse design and flexible parameterization of meta-optics using algorithmic differentiation,” Commun. Phys. **4**, 1–11 (2021).
18. P. R. Wiecha, A. Arbouet, C. Girard, and O. L. Muskens, “Deep learning in nano-photonics: inverse design and beyond,” Photon. Res. **9**, B182–B200 (2021).
19. A. Sinatra, C. Lobo, and Y. Castin, “The truncated Wigner method for Bose-condensed gases: limits of validity and applications,” J. Phys. B **35**, 3599 (2002).
20. E. Brambilla, A. Gatti, M. Bache, and L. A. Lugiato, “Simultaneous near-field and far-field spatial quantum correlations in the high-gain regime of parametric down-conversion,” Phys. Rev. A **69**, 023802 (2004).
21. J. Corney and M. Olsen, “Non-Gaussian pure states and positive Wigner functions,” Phys. Rev. A **91**, 023824 (2015).
22. R. Lewis-Swan, M. Olsen, and K. Kheruntsyan, “Approximate particle number distribution from direct stochastic sampling of the Wigner function,” Phys. Rev. A **94**, 033814 (2016).
23. P. Drummond, “Higher-order stochastic differential equations and the positive Wigner function,” Phys. Rev. A **96**, 062104 (2017).
24. J. Weinbub and D. Ferry, “Recent advances in Wigner function approaches,” Appl. Phys. Rev. **5**, 041104 (2018).
25. S. Trajtenberg-Mills, A. Karnieli, N. Voloch-Bloch, E. Megidish, H. S. Eisenberg, and A. Arie, “Simulating correlations of structured spontaneously down-converted photon pairs,” Laser Photon. Rev. **14**, 1900321 (2020).
26. M. O. Scully and M. S. Zubairy, *Quantum Optics* (1999).
27. J. Garrison and R. Chiao, *Quantum Optics* (Oxford University, 2008).
28. R. Ursin, F. Tiefenbacher, T. Schmitt-Manderbach, H. Weier, T. Scheidl, M. Lindenthal, B. Blauensteiner, T. Jennewein, J. Perdigues, P. Trojek, B. Ömer, M. Fürst, M. Meyenburg, J. Rarity, Z. Sodnik, C. Barbieri, H. Weinfurter, and A. Zeilinger, “Entanglement-based quantum communication over 144 km,” Nat. Phys. **3**, 481–486 (2007).
29. N. Gisin and R. Thew, “Quantum communication,” Nat. Photonics **1**, 165–171 (2007).
30. G. Vallone, D. Bacco, D. Dequal, S. Gaiarin, V. Luceri, G. Bianco, and P. Villoresi, “Experimental satellite quantum communications,” Phys. Rev. Lett. **115**, 040502 (2015).
31. Y.-A. Chen, Q. Zhang, T.-Y. Chen, *et al.*, “An integrated space-to-ground quantum communication network over 4,600 kilometres,” Nature **589**, 214–219 (2021).
32. E. Knill, R. Laflamme, and G. J. Milburn, “A scheme for efficient quantum computation with linear optics,” Nature **409**, 46–52 (2001).
33. P. Kok, W. J. Munro, K. Nemoto, T. C. Ralph, J. P. Dowling, and G. J. Milburn, “Linear optical quantum computing with photonic qubits,” Rev. Mod. Phys. **79**, 135 (2007).
34. J. B. Spring, B. J. Metcalf, P. C. Humphreys, W. S. Kolthammer, X.-M. Jin, M. Barbieri, A. Datta, N. Thomas-Peter, N. K. Langford, D. Kundys, J. C. Gates, B. J. Smith, P. G. R. Smith, and I. A. Walmsley, “Boson sampling on a photonic chip,” Science **339**, 798–801 (2013).
35. H.-S. Zhong, H. Wang, Y.-H. Deng, *et al.*, “Quantum computational advantage using photons,” Science **370**, 1460–1463 (2020).
36. C. H. Bennett, F. Bessette, G. Brassard, L. Salvail, and J. Smolin, “Experimental quantum cryptography,” J. Cryptol. **5**, 3–28 (1992).
37. C. H. Bennett and G. Brassard, “Quantum cryptography: public key distribution and coin tossing,” Theoretical Computer Science **560**, 7–11 (2020).
38. A. Sit, F. Bouchard, R. Fickler, J. Gagnon-Bischoff, H. Larocque, K. Heshami, D. Elser, C. Peuntinger, K. Günthner, B. Heim, C. Marquardt, G. Leuchs, R. W. Boyd, and E. Karimi, “High-dimensional intracity quantum cryptography with structured photons,” Optica **4**, 1006–1010 (2017).
39. S.-K. Liao, W.-Q. Cai, W.-Y. Liu, L. Zhang, Y. Li, J.-G. Ren, J. Yin, Q. Shen, Y. Cao, and Z.-P. Li, “Satellite-to-ground quantum key distribution,” Nature **549**, 43–47 (2017).
40. S. Pirandola, U. L. Andersen, L. Banchi, M. Berta, D. Bunandar, R. Colbeck, D. Englund, T. Gehring, C. Lupo, C. Ottaviani, J. Pereira, M. Razavi, J. S. Shaari, M. Tomamichel, V. C. Usenko, G. Vallone, P. Villoresi, and P. Wallden, “Advances in quantum cryptography,” Adva. Opt. Photon. **12**, 1012–1236 (2020).
41. R. W. Boyd, *Nonlinear Optics* (Academic, 2020).
42. C. Couteau, “Spontaneous parametric down-conversion,” Contemp. Phys. **59**, 291 (2018).
43. V. Berger, “Nonlinear photonic crystals,” Phys. Rev. Lett. **81**, 4136 (1998).
44. N. Broderick, G. Ross, H. Offerhaus, D. Richardson, and D. Hanna, “Hexagonally poled lithium niobate: a two-dimensional nonlinear photonic crystal,” Phys. Rev. Lett. **84**, 4345 (2000).
45. T. Xu, K. Switkowski, X. Chen, S. Liu, K. Koynov, H. Yu, H. Zhang, J. Wang, Y. Sheng, and W. Krolikowski, “Three-dimensional nonlinear photonic crystal in ferroelectric barium calcium titanate,” Nat. Photonics **12**, 591–595 (2018).
46. D. Wei, C. Wang, H. Wang, X. Hu, D. Wei, X. Fang, Y. Zhang, D. Wu, Y. Hu, J. Li, S. Zhu, and M. Xiao, “Experimental demonstration of a three-dimensional lithium niobate nonlinear photonic crystal,” Nat. Photonics **12**, 596–600 (2018).

47. S. Liu, K. Switkowski, C. Xu, J. Tian, B. Wang, P. Lu, W. Krolikowski, and Y. Sheng, "Nonlinear wavefront shaping with optically induced three-dimensional nonlinear photonic crystals," Nat. Commun. **10**, 3208 (2019).
48. D. Wei, C. Wang, X. Xu, H. Wang, Y. Hu, P. Chen, J. Li, Y. Zhu, C. Xin, X. Hu, Y. Zhang, D. Wu, J. Chu, S. Zhu, and M. Xiao, "Efficient nonlinear beam shaping in three-dimensional lithium niobate nonlinear photonic crystals," Nat. Commun. **10**, 4193 (2019).
49. J. Imbrock, L. Wesemann, S. Kroesen, M. Ayoub, and C. Denz, "Waveguide-integrated three-dimensional quasi-phase-matching structures," Optica **7**, 28–34 (2020).
50. S. Liu, L. M. Mazur, W. Krolikowski, and Y. Sheng, "Nonlinear volume holography in 3D nonlinear photonic crystals," Laser Photon. Rev. **14**, 2000224 (2020).
51. Y. Zhang, Y. Sheng, S. Zhu, M. Xiao, and W. Krolikowski, "Nonlinear photonic crystals: from 2D to 3D," Optica **8**, 372–381 (2021).
52. P. Chen, C. Wang, D. Wei, *et al.*, "Quasi-phase-matching-division multiplexing holography in a three-dimensional nonlinear photonic crystal," Light Sci. Appl. **10**, 146 (2021).
53. A. Arie, "Storing and retrieving multiple images in 3D nonlinear photonic crystals," Light Sci. Appl. **10**, 202 (2021).
54. S. Walborn and A. Pimentel, "Generalized Hermite–Gauss decomposition of the two-photon state produced by spontaneous parametric down conversion," J. Phys. B **45**, 165502 (2012).
55. M. Malik, M. Erhard, M. Huber, M. Krenn, R. Fickler, and A. Zeilinger, "Multi-photon entanglement in high dimensions," Nat. Photonics **10**, 248–252 (2016).
56. A. Dosseva, Ł. Cincio, and A. M. Brańczyk, "Shaping the joint spectrum of down-converted photons through optimized custom poling," Phys. Rev. A **93**, 013801 (2016).
57. E. Kovlakov, I. Bobrov, S. Straupe, and S. Kulik, "Spatial Bell-state generation without transverse mode subspace postselection," Phys. Rev. Lett. **118**, 030503 (2017).
58. M. Erhard, R. Fickler, M. Krenn, and A. Zeilinger, "Twisted photons: new quantum perspectives in high dimensions," Light Sci. Appl. **7**, 17146 (2018).
59. E. V. Kovlakov, S. S. Straupe, and S. P. Kulik, "Quantum state engineering with twisted photons via adaptive shaping of the pump beam," Phys. Rev. A **98**, 060301 (2018).
60. C. Cui, R. Arian, S. Guha, N. Peyghambarian, Q. Zhuang, and Z. Zhang, "Wave-function engineering for spectrally uncorrelated biphotons in the telecommunication band based on a machine-learning framework," Phys. Rev. Appl. **12**, 034059 (2019).
61. M. Erhard, M. Krenn, and A. Zeilinger, "Advances in high-dimensional quantum entanglement," Nat. Rev. Phys. **2**, 365–381 (2020).
62. P. Boucher, H. Defienne, and S. Gigan, "Engineering spatial correlations of entangled photon pairs by pump beam shaping," Opt. Lett. **46**, 4200–4203 (2021).
63. F. Brandt, M. Hiekkamäki, F. Bouchard, M. Huber, and R. Fickler, "High-dimensional quantum gates using full-field spatial modes of photons," Optica **7**, 98–107 (2020).
64. M. Krenn, J. Handsteiner, M. Fink, R. Fickler, and A. Zeilinger, "Twisted photon entanglement through turbulent air across Vienna," Proc. Natl. Acad. Sci. USA **112**, 14197–14201 (2015).
65. A. Sit, R. Fickler, F. Alsaiari, F. Bouchard, H. Larocque, P. Gregg, L. Yan, R. W. Boyd, S. Ramachandran, and E. Karimi, "Quantum cryptography with structured photons through a vortex fiber," Opt. Lett. **43**, 4108–4111 (2018).
66. E. De Bézenac, A. Pajot, and P. Gallinari, "Deep learning for physical processes: incorporating prior scientific knowledge," J. Stat. Mech. Theory Exp. **2019**, 124009 (2019).
67. G. Pang and G. E. Karniadakis, "Physics-informed learning machines for partial differential equations: Gaussian processes versus neural networks," in *Emerging Frontiers in Nonlinear Science* (Springer, 2020), pp. 323–343.
68. J. Sirignano, J. F. MacArt, and J. B. Freund, "DPM: a deep learning PDE augmentation method with application to large-Eddy simulation," J. Comput. Phys. **423**, 109811 (2020).
69. S. Pakravan, P. A. Mistani, M. A. Aragon-Calvo, and F. Gibou, "Solving inverse-PDE problems with physics-aware neural networks," J. Comput. Phys. **440**, 110414 (2021).
70. J. Torres, A. Alexandrescu, and L. Torner, "Quantum spiral bandwidth of entangled two-photon states," Phys. Rev. A **68**, 050301 (2003).
71. M. I. Kolobov, "The spatial behavior of nonclassical light," Rev. Mod. Phys. **71**, 1539 (1999).
72. K. Binder, D. Heermann, L. Roelofs, A. J. Mallinckrodt, and S. McKay, "Monte Carlo simulation in statistical physics," Comput. Phys. **7**, 156–157 (1993).
73. P. Stoffa, J. T. Fokkema, R. de Luna Freire, and W. Kessinger, "Split-step Fourier migration," Geophysics **55**, 410–421 (1990).
74. G. D. Domenico, S. Pearl, A. Karnieli, S. Trajtenberg-Mills, I. Juwiler, H. S. Eisenberg, and A. Arie, "High efficiency generation of path entangled bi-photons directly from 2D poled nonlinear crystal," in *OSA Nonlinear Optics* (Optical Society of America, 2021), paper NM2B.2.
75. G. D. Domenico, S. Pearl, A. Karnieli, S. Trajtenberg-Mills, I. Juwiler, H. S. Eisenberg, and A. Arie, "Video presentation of high efficiency generation of path entangled bi-photons directly from 2D poled nonlinear crystal, minute 4:50," 2021, https://doi.org/10.1364/NLO.2021.NM2B.2.
76. A. Mair, A. Vaziri, G. Weihs, and A. Zeilinger, "Entanglement of the orbital angular momentum states of photons," Nature **412**, 313–316 (2001).
77. A. Chowdhury, C. Staus, B. F. Boland, T. F. Kuech, and L. McCaughan, "Experimental demonstration of 1535–1555-nm simultaneous optical wavelength interchange with a nonlinear photonic crystal," Opt. Lett. **26**, 1353–1355 (2001).
78. T. Ellenbogen, N. Voloch-Bloch, A. Ganany-Padowicz, and A. Arie, "Nonlinear generation and manipulation of Airy beams," Nat. Photonics **3**, 395–398 (2009).
79. N. V. Bloch, K. Shemer, A. Shapira, R. Shiloh, I. Juwiler, and A. Arie, "Twisting light by nonlinear photonic crystals," Phys. Rev. Lett. **108**, 233902 (2012).
80. A. Shapira, R. Shiloh, I. Juwiler, and A. Arie, "Two-dimensional nonlinear beam shaping," Opt. Lett. **37**, 2136–2138 (2012).
81. X.-H. Hong, B. Yang, C. Zhang, Y.-Q. Qin, and Y.-Y. Zhu, "Nonlinear volume holography for wave-front engineering," Phys. Rev. Lett. **113**, 163902 (2014).
82. B. Zhu, H. Liu, Y. Chen, and X. Chen, "High conversion efficiency second-harmonic beam shaping via amplitude-type nonlinear photonic crystals," Opt. Lett. **45**, 220–223 (2020).
83. E. Rozenberg, "JAX implementation for learning 3D nonlinear photonic crystals and pump structure for high-dimensional quantum state engineering," Github, 2021, https://github.com/EyalRozenberg1/SPDCinv.
84. E. Rozenberg, A. Karnieli, O. Yesharim, S. Trajtenberg-Mills, D. Freedman, A. M. Bronstein, and A. Arie, "Inverse design of quantum holograms in three-dimensional nonlinear photonic crystals," in *Conference on Lasers and Electro-Optics (CLEO)* (Optica Publishing Group, 2021), FM1N.7.
85. S. Arora, S. Du, W. Hu, Z. Li, and R. Wang, "Fine-grained analysis of optimization and generalization for overparameterized two-layer neural networks," in *International Conference on Machine Learning* (PMLR, 2019), pp. 322–332.
86. K. Lyu, Z. Li, R. Wang, and S. Arora, "Gradient descent on two-layer nets: margin maximization and simplicity bias," in *Advances in Neural Information Processing Systems 34 (NeurIPS 2021)* (Curran Associates, Inc., 2021), p. 12978.
87. R. C. Aster, B. Borchers, and C. H. Thurber, *Parameter Estimation and Inverse Problems* (Elsevier, 2018).
88. G. Imeshev, M. Arbore, M. Fejer, A. Galvanauskas, M. Fermann, and D. Harter, "Ultrashort-pulse second-harmonic generation with longitudinally nonuniform quasi-phase-matching gratings: pulse compression and shaping," J. Opt. Soc. Am. B **17**, 304–318 (2000).
89. J. D. Bierlein and H. Vanherzeele, "Potassium titanyl phosphate: properties and new applications," J. Opt. Soc. Am. B **6**, 622–633 (1989).
90. M. Leidinger, S. Fieberg, N. Waasem, F. Kühnemann, K. Buse, and I. Breunig, "Comparative study on three highly sensitive absorption measurement techniques characterizing lithium niobate over its entire transparent spectral range," Opt. Express **23**, 21690–21705 (2015).
91. M. Werner, M. Raymer, M. Beck, and P. Drummond, "Ultrashort pulsed squeezing by optical parametric amplification," Phys. Rev. A **52**, 4202 (1995).
92. M. Werner and P. Drummond, "Pulsed quadrature-phase squeezing of solitary waves in $\chi^{(2)}$ parametric waveguides," Phys. Rev. A **56**, 1508 (1997).
93. P. D. Drummond, B. Opanchuk, A. Dellios, and M. D. Reid, "Simulating complex networks in phase space: Gaussian boson sampling," Phys. Rev. A **105**, 012427 (2022).

94. K. Gregor and Y. LeCun, "Learning fast approximations of sparse coding," in *Proceedings of the 27th International Conference on International Conference on Machine Learning* (2010), pp. 399–406.
95. G. Agrawal, *Applications of Nonlinear Fiber Optics* (Elsevier, 2001).
96. S. Rana, P. Parashar, and M. Lewenstein, "Trace-distance measure of coherence," Phys. Rev. A **93**, 012110 (2016).
97. J. Bradbury, R. Frostig, P. Hawkins, M. J. Johnson, C. Leary, D. Maclaurin, G. Necula, A. Paszke, J. VanderPlas, S. Wanderman-Milne, and Q. Zhang, "JAX: composable transformations of Python+NumPy programs," Github, 2018, http://github.com/google/jax.
98. L.-A. Wu, H. Kimble, J. Hall, and H. Wu, "Generation of squeezed states by parametric down conversion," Phys. Rev. Lett. **57**, 2520 (1986).
99. C. Gardiner and P. Zoller, *Quantum Noise: A Handbook of Markovian and Non-Markovian Quantum Stochastic Methods with Applications to Quantum Optics* (Springer, 2004).
100. T. T. Georgiou and A. Lindquist, "Kullback-Leibler approximation of spectral density functions," IEEE Trans. Inf. Theory **49**, 2910–2917 (2003).
101. E. Giné, D. M. Mason, and A. Y. Zaitsev, "The $\{L_1\}$-norm density estimator process," Ann. Probab. **31**, 719–768 (2003).
102. R. Thew, K. Nemoto, A. G. White, and W. J. Munro, "Qudit quantum-state tomography," Phys. Rev. A **66**, 012303 (2002).
103. M. Agnew, J. Leach, M. McLaren, F. S. Roux, and R. W. Boyd, "Tomography of the quantum state of photons entangled in high dimensions," Phys. Rev. A **84**, 062101 (2011).
104. E. Toninelli, B. Ndagano, A. Vallés, B. Sephton, I. Nape, A. Ambrosio, F. Capasso, M. J. Padgett, and A. Forbes, "Concepts in quantum state tomography and classical implementation with intense light: a tutorial," Adv. Opt. Photon. **11**, 67–134 (2019).
105. P. Kazansky and V. Pruneri, "Electric-field poling of quasi-phase-matched optical fibers," J. Opt. Soc. Am. B **14**, 3170–3179 (1997).
106. C. A. Fuchs, N. Gisin, R. B. Griffiths, C.-S. Niu, and A. Peres, "Optimal eavesdropping in quantum cryptography. I. Information bound and optimal strategy," Phys. Rev. A **56**, 1163 (1997).
107. T. Durt, D. Kaszlikowski, J.-L. Chen, and L. C. Kwek, "Security of quantum key distributions with entangled qudits," Phys. Rev. A **69**, 032313 (2004).
108. K. Zielnicki, K. Garay-Palmett, D. Cruz-Delgado, H. Cruz-Ramirez, M. F. O'Boyle, B. Fang, V. O. Lorenz, A. B. U'Ren, and P. G. Kwiat, "Joint spectral characterization of photon-pair sources," J. Mod. Opt. **65**, 1141–1160 (2018).
109. Y. Qi and Y. Li, "Integrated lithium niobate photonics," Nanophotonics **9**, 1287–1320 (2020).
110. J. E. Sharping, K. F. Lee, M. A. Foster, A. C. Turner, B. S. Schmidt, M. Lipson, A. L. Gaeta, and P. Kumar, "Generation of correlated photons in nanoscale silicon waveguides," Opt. Express **14**, 12388–12393 (2006).
111. G. I. Stegeman and M. Segev, "Optical spatial solitons and their interactions: universality and diversity," Science **286**, 1518–1523 (1999).
112. Z. Chen, M. Segev, and D. N. Christodoulides, "Optical spatial solitons: historical overview and recent advances," Rep. Prog. Phys. **75**, 086401 (2012).
113. G. P. Agrawal, "Nonlinear fiber optics," in *Nonlinear Science at the Dawn of the 21st Century*, P. L. Christiansen, M. P. Sørensen, and A. C. Scott, eds. (Springer, 2000), pp. 195–211.
114. C. Häger and H. D. Pfister, "Physics-based deep learning for fiber-optic communication systems," IEEE J. Sel. Areas Commun. **39**, 280–294 (2020).
115. W. Wasilewski, C. Radzewicz, R. Frankowski, and K. Banaszek, "Statistics of multiphoton events in spontaneous parametric down-conversion," Phys. Rev. A **78**, 033831 (2008).
116. P. Coleman, *Introduction to Many-Body Physics* (Cambridge University, 2015).